

Injection current in ferroelectric group-IV monochalcogenide monolayers

Suman Raj Panday,¹ Salvador Barraza-Lopez,² Tonatiuh Rangel,³ and Benjamin M. Fregoso¹

¹*Department of Physics, Kent State University, Kent OH, 44242, USA*

²*Department of Physics, University of Arkansas, Fayetteville AR, 72701, USA*

³*Department of Physics, University of California, Berkeley CA, 94720, USA*

We study the injection current susceptibility tensor (also known as the circular photogalvanic effect) of ferroelectric single-layer GeS, GeSe, SnS, and SnSe. We find that the injection current is perpendicular to the spontaneous in-plane polarization, can reach effective values of the order of 10^{10} A/V²s, and peaks at photon energies in the visible spectrum. The magnitude is the largest reported in the literature so far. To rationalize our results, we construct a simple two-band model of injection current. Analysis of the model suggests that two-dimensions, in-plane polarization, mirror symmetry, large hopping integrals, and valence (v) and conduction (c) band center separation are important factors determining the magnitude and direction of the injection current. Our results also suggest strain as a control knob of injection current in optoelectronic applications of these materials.

I. INTRODUCTION

Understanding the nonlinear optical response of materials is of great practical significance. The injection current, for example, is a second order optical effect which has attracted attention for its role in the photovoltaic (PV) effect of ferroelectric (FE) materials¹, in solar cell technology^{1,2}, coherent current control^{3,4}, and in the band topology of materials⁵.

The PV effect in FE materials, the so-called bulk photovoltaic effect (BPVE), is distinct from other PV phenomena because it does not require semiconductor pn-junctions, and photovoltages can be many times larger than the energy gaps of the semiconductors involved⁶. In addition, the BPVE may play a role in the PV mechanism of the highly-efficient, potentially low-cost, hybrid perovskite solar cells some of which are FE².

The injection current was first identified as one component of the BPVE¹. The other component being the shift current^{1,4,7}. The injection current is also called circular photogalvanic effect because it vanishes for linear polarization of light; or ballistic current because transport occurs before momentum relaxation, e.g., it is a ‘hot’ electron effect. The injection current is ‘classical’ in the sense that it depends only on the diagonal elements of the density matrix (occupations), whereas the shift current is quantum in the sense that it depends only on the off-diagonal elements of the density matrix^{4,7}.

Being a second order effect in the electric field, the injection current is nonzero in materials lacking inversion center. The lack of inversion symmetry manifests in two distinct scenarios. In one scenario, photoexcited carriers experience asymmetric momentum relaxation in the $\pm\mathbf{k}$ directions leading to a polar distribution and a net current¹. The origin of such asymmetric relaxation could be phonons, impurities, etc. The derivation of the injection current in this case starts from a kinetic equation. In the second scenario, photoexcited carriers are pumped into $\pm\mathbf{k}$ -points of the Brillouin zone (BZ) at different rates leading to a polar distribution of velocity states and hence to a charge current⁴. The starting

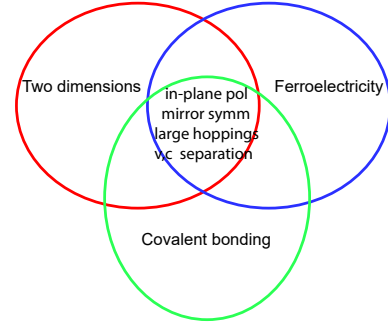


FIG. 1. Conceptual diagram showing the important factors contributing to large injection current susceptibility tensor in two-dimensional (2D) ferroelectric (FE) single-layer GeS, GeSe, SnS and SnSe. These are in-plane polarization, mirror symmetry, large hopping integrals, and valence (v) and conduction (c) band center separation, which lie at the intersection of materials with 2D ferroelectricity with strong covalent bonding.

point is a Hamiltonian coupled to light and momentum relaxation is usually added *a posteriori*. The key point in both scenarios is the unequal scattering rates in distinct directions in momentum. In the relaxation-time approximation, both scenarios give the same expression for the current. In this article we study the injection current from the perspective of the second scenario.

Although progress in FE-based solar cells has been made^{8,9}, the photocurrents are still small resulting in smaller efficiencies compared with conventional Si-based cells. Group-IV monolayer monochalcogenides (MMs) GeS, GeSe, SnS and SnSe are predicted to be a new class of 2D materials with energy gaps in the visible regime and other novel mechanical and optical properties^{10–12}. Below a critical temperature^{13–15} they become FE hence providing a new playground to study the effects of polarization on shift and injection current, i.e., on the BPVE.

Injection and shift current usually occur simultaneously and distinguishing one from another is challenging⁹. The shift current in MMs was recently studied

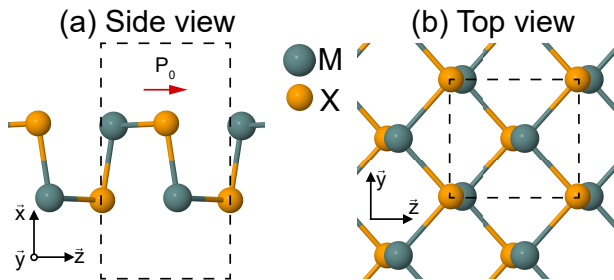


FIG. 2. (a) Structure of monochalcogenide monolayers (MMs); $M=\text{Ge, Sn}$ $X=\text{S, Se}$. (b) The unit cell contains 4 atoms and is indicated within boxes. The point group lacks an inversion center and develops a nonzero in-plane spontaneous polarization P_0 .

theoretically using first-principles density functional theory (DFT)^{16,17} and experimentally using Terahertz spectroscopy in the group of L. Titova^{18,19}. It was found to be large, potentially able to overcome the limitation of bulk FEs. However, to understand the BPVE, the injection current in 2D FEs must be studied in detail. For example, whether injection current is large in 2D MMs or how it can be engineered is unknown and would lead to a better understanding of light-matter interactions and novel optoelectronic applications.

Naively we expect that the more light absorbed by the material the larger the injection current. Since the imaginary part of the dielectric function governs the optical absorption, the injection current would follow the joint density of states (JDOS), e.g. peaks at van Hove singularities. In addition, the injection current is not expected to strongly depend on the polarization. Contrary to shift current, the injection current does not introduce a length scale into the transport problem^{4,7} which could be naively associated with a microscopic dipole of the FE phase.

In this work, we test these ideas using analytic and numerical methods. We study correlations between the injection current, the imaginary part of the dielectric function, and the spontaneous polarization (or strain). We find that the injection current susceptibility tensor could reach effective values of the order 10^{10} A/V²s, which is the largest reported so far, see Table I, and is the largest for photon energies corresponding to the visible light spectrum, establishing the potential of these materials for optoelectronic applications.

We also find that optical absorption does not play a big role in determining the magnitude of the injection current but polarization does. To ascertain the role of polarization, we compare the frequency-averaged injection current with, i) the polarization of a particular material with various atomic positions along a path in configuration space (this could also be interpreted as straining the material) and ii) the polarization across materials. From i), we find the injection current susceptibility tensor is nonmonotonic with respect to polarization (strain), with

an optimal value giving the maximum average current. From ii) we find that the higher the spontaneous polarization of the material, the higher the injection current.

To understand if polarization plays a causal role, we construct a simple two-band model of injection current in which the factors that contribute to the injection current can be disentangled. The analysis of the model pointed to, i) the 2D nature of the material, ii) the FE character, and iii) the covalent bonding as the main factors determining the magnitude of the injection current susceptibility tensor, Fig. 1.

This paper is organized as follows. In Sec. II we describe the numerical procedure. In Sec. III we preset the DFT injection current, optical absorption, polarization, and their correlations. In Sec. IV we introduce a simple two-band model for the injection current and conclude in Sec. V.

II. NUMERICAL METHODS

We use density functional theory (DFT) as implemented in the ABINIT²⁰ computer package, with the generalized gradient approximation to the exchange correlation energy functional as implemented by Perdew, Burke and Ernzerhof.²¹ Hartwigsen-Goedecker-Hutter norm conserving pseudo potentials²² were employed. To expand the plane waves basis set, energy cutoffs of 50 Hartrees were employed for GeS and GeSe, and 60 Hartrees for SnS and SnSe. We set a separation of 15 Å along the x -direction in Fig. 2, which makes for more than 10 Å of vacuum among periodic images. To calculate the injection current, we included 20 valence and 30 conduction bands for GeS and SnS, and 30 valence and 20 conduction bands for GeSe and SnSe. They account for all allowed transitions up to 6 eV.

To extract the effective response of a single-layer, we scale the numerical result by the factor L/d , where L is the supercell lattice parameter perpendicular to the slab, and d is the effective thickness of the monolayer. For concreteness, we estimate the slab thicknesses as 2.56, 2.59, 2.85 and 2.76 Å for GeS, GeSe, SnS, and SnSe, respectively. Once the ground-state wave function and energies were computed, the TINIBA package²³ was used to compute the injection current susceptibility η_2^{abc} as implemented in Ref. 4. The sum over \mathbf{k} -points is made using the interpolation tetrahedron method²⁴. See the Appendices for mode details.

III. NUMERICAL RESULTS

A. Injection current

An incident monochromatic optical field $E^a = E^a(\omega)e^{-i\omega t} + \text{c.c.}$ induces an injection current governed

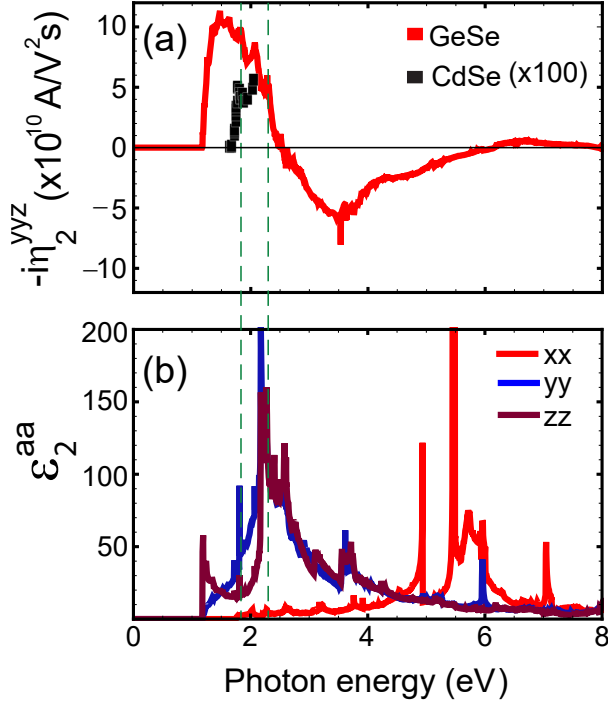


FIG. 3. (a) Injection current susceptibility tensor of single-layer GeSe (red line) and CdSe (black squares)²⁵. The injection current of GeSe is two orders of magnitude larger than that of CdSe and peaks for photon energies in the visible spectrum. The large magnitude of the injection current in the visible light spectrum highlights the potential of these materials for optoelectronic applications. (b) Imaginary part of the dielectric function, Eq. 4. There is not an obvious correlation with injection current.

by the equation

$$\frac{d}{dt} J_{inj}^a = 2\eta_2^{abc} E^b(\omega) E^c(-\omega) - \frac{J_{inj}^a}{\tau}. \quad (1)$$

τ is a phenomenological momentum relaxation time and $\eta_2^{abc}(0, \omega, -\omega)$ is the injection current tensor^{1,4}

$$\eta_2^{abc} = \frac{e^3 \pi}{2\hbar^2 V} \sum_{nm\mathbf{k}} \omega_{mn,a} f_{nm} [r_{mn}^c, r_{nm}^b] \delta(\omega_{mn} - \omega), \quad (2)$$

where $a, b, c = x, y, z$ are Cartesian components, n is the band index, $f_{nm} = f_n - f_m$ is the difference in occupation numbers at zero temperature of bands n and m , $\hbar\omega_n$ is the energy of the band n , $r_{nm}^a = i\langle u_n | u_{m,a} \rangle$ are the Berry connections, u_n the periodic part of the Bloch wavefunction, $[r_{mn}^c, r_{nm}^b] \equiv r_{mn}^c r_{nm}^b - r_{mn}^b r_{nm}^c$, and summation over repeated indices is implied. We define the subscript X_a to mean derivative with respect to the crystal momentum with Cartesian coordinate a . For example, $\omega_{nm,a} \equiv (\omega_n - \omega_m)_{,a} = \omega_{n,a} - \omega_{m,a} = v_n^a - v_m^a$ are band-velocity differences. In the thermodynamic limit in d -dimensions we have $(1/V) \sum_{\mathbf{k}} \rightarrow \int d\mathbf{k} / (2\pi)^d$, where the integral is over the (BZ) and V is the sample volume.

| Material | $ \eta_2 $ ($\times 10^8$ A/V ² s) | $\hbar\omega$ (eV) | P_0 ($\mu\text{C}/\text{cm}^2$) | Ref. |
|----------|---|-----------------------|--|----------|
| MX | 100-1000 | 1.5-2.5 | 72-195 [16] | present |
| CdSe | 7 | 2.2 | 0.6 [26] | 27(th.) |
| CdS | 4 | 2.8 | | 27(th.) |
| CdSe | 5 | 2 | 0.6 [26] | 25(exp.) |
| CdSe | 1.5 | 1.8 | 0.6 [26] | 28(exp.) |
| CdS | 4 | 3 | | 28(exp.) |

TABLE I. Reported estimates of the injection current susceptibility tensors in various materials. The photon energy, spontaneous polarization $|\mathbf{P}_0| = P_0$, theoretical (th.), and experimental (exp.) values are indicated. MX stands for single-layer GeS, GeSe, SnS or SnSe and in this case effective (bulk) values are given.

η_2^{abc} is a third rank tensor antisymmetric in the last two indices. It vanishes for linearly polarized light, and this is why the effect we are describing receives the alternative name of a circular photogalvanic effect. The MMs have a point group of $mm2$ which contains a two-fold (polar) axis, two mirror plane symmetries, and lacks center of inversion. Accordingly, the nonzero components of η_2 are $xxx, zyy, zzz, yyz, xzx, xxz$ and yzx . Antisymmetry of η_2 with respect to exchange of the last two indices implies that the zzx, zzy, zzz components vanish. There are two independent components yyz, xzx out of the four remaining ones. However, the plane of the slab is perpendicular to the x -axis, Fig. 2, and hence the component xxz is much smaller than the yyz component. Here we focus on the yyz component given by

$$\eta_2^{yyz} = \frac{e^3 \pi}{2\hbar^2 V} \sum_{nm\mathbf{k}} \omega_{mn,y} f_{nm} [r_{mn}^z, r_{nm}^y] \delta(\omega_{mn} - \omega). \quad (3)$$

Note that the injection current flows in the plane of the MMs and perpendicular to the spontaneous polarization $\mathbf{P}_0 = \hat{z}P_0$. In Fig. 3(a) we show the injection current for the GeSe monolayer as a function of incident photon energy $\hbar\omega$. The response of other materials is similar and presented in Appendix B. Notice that the injection current susceptibility tensor is of order 10^{10} A/V²s and peaks in the visible light spectrum (1.5 – 3 eV). As the photon energy increases, the injection reverses its direction several times and progressively decreases in magnitude. To give perspective of this value, the reported injection current susceptibility tensors for other prototypical semiconductors is two orders of magnitude smaller, see Table I, highlighting the actual potential of MMs for optoelectronic applications.

B. Linear dielectric function

In order to understand the origin of the large injection current, we first compare it with the imaginary part of

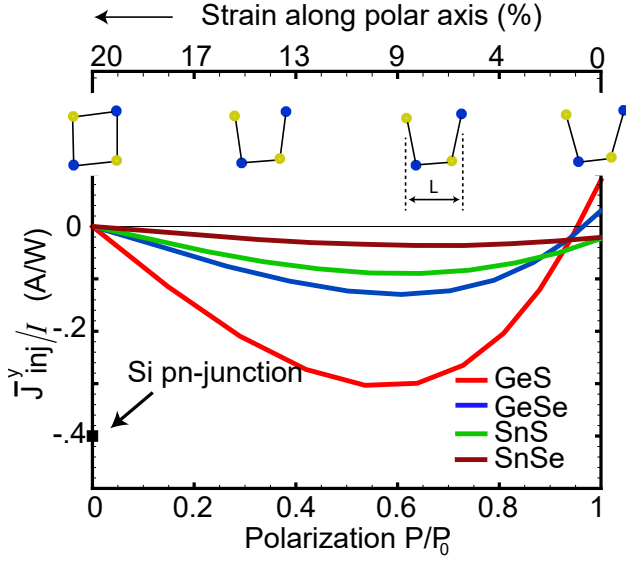


FIG. 4. Average current per unit incident intensity (I) and the polarization (strain) for various materials. For a given material, the average current is nonmonotonic, with a given value of polarization(strain) yielding maximum photocurrent. On the other hand, the larger the *spontaneous* polarization of a material (P_0) the larger the magnitude of the injection current. This implies that spontaneous polarization plays a role in generating large injection current. To calculate the current we use reasonable parameters for clean semiconductors $\tau = 100$ fs [29], $\epsilon/\epsilon_0 \sim 4$ [10], $W = 10$ eV. The magnitude of the current obtained is close to the state of the art Si-based solar cells of 400 mA/W^{30} .

the linear dielectric function

$$\epsilon_2^{ab} = \frac{4e^2\pi^2}{\epsilon_0\hbar V} \sum_{nm\mathbf{k}} f_{nm} r_{nm}^a r_{mn}^b \delta(\omega_{mn} - \omega), \quad (4)$$

which governs the optical absorption of the material and whose frequency dependence (mostly) follows the JDOS. Our linear response calculation, shown in Fig. 3(b), agrees with previous reports^{10,16}. Higher ϵ_2 leads to higher light absorption, in particular, at frequencies near the van Hove peaks. If light absorption were the origin of the large injection current, its frequency dependence would correlate with that of ϵ_2 . Inspection of Fig. 3(b) shows that few peaks in the injection current match the energy locations of van Hove singularities in ϵ_2 (two of them indicated by dashed vertical lines). This indicates that neither the magnitude nor the direction of the injection current could be explained by light absorption alone.

Contrary to the shift current, the injection current does not introduce an intrinsic length scale into the transport problem. If it did, such a length scale would be naively associated with the size of a dipole moment of the FE material. Since it does not, we do not expect the injection current to depend strongly on polarization. To test this idea, we compare the average current (defined be-

low) with the material's polarization for i) each material as we vary its atomic positions and ii) across materials which have different *spontaneous* polarizations.

C. Average current

From Eq. 1, a circularly polarized optical field induces a current given by

$$\frac{d}{dt} J_{inj}^y = \pm i \eta_2^{yyz} |E_0|^2 - J_{inj}^y / \tau, \quad (5)$$

where \pm determines the chirality of light and E_0 is the amplitude of the optical field. We used the convention in which $E^a(\omega) = E_0^a/2$ [31]. In steady state, the injection current is $J_{inj}^y = \pm \tau i \eta_2^{yyz} |E_0|^2$. If the light was composed of a broad range of frequencies with equal intensity (white light), we would expect the measured current would be an average over the frequencies

$$\bar{J}_{inj}^y = \frac{1}{\Delta\Omega} \int_0^W d\omega J_{inj}^y, \quad (6)$$

where $\hbar\Delta\Omega = (W - E_g)$ and W is the range of the light spectrum.

D. Electric polarization and strain

We compute polarization for each material at various atomic positions along a path in configuration space starting from the centrosymmetric configuration, with zero polarization, and ending in the ground state configuration, with its spontaneous polarization. The electric polarization^{32,33}

$$\mathbf{P}(\lambda) = \frac{e}{V} \sum_i Z^i \mathbf{r}_i(\lambda) - \frac{e}{V} \sum_{v\mathbf{k}} \boldsymbol{\xi}_{vv}(\lambda), \quad (7)$$

has ionic and electronic components represented by the first and second terms above. $\boldsymbol{\xi}_{vv}(\lambda) = i \langle u_v^\lambda | u_{v,a}^\lambda \rangle$ is the Berry connection and summation is over occupied states. The details of the calculation are presented in Appendix C.

λ parametrizes the path. Note that the motion of the atoms occurs only along the z -direction, see Table III. This is equivalent to straining the lattice along the polar axis. To quantify the strain we define

$$\text{strain} = \frac{L - L_0}{L_0} \quad (8)$$

where L is the distance between the Ge-Se atoms in the unit cell (see fig. 4) and L_0 is the distance in the ground state.

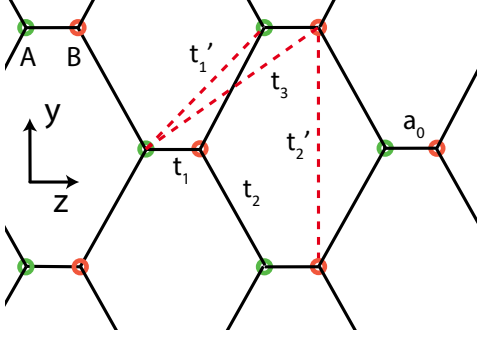


FIG. 5. Tight-binding (TB) model for calculating injection current in single-layer GeS. The lattice has two nonequivalent sites (A, B) per unit cell and the hoppings parameters are indicated. The crystal lacks inversion symmetry and develops spontaneous polarization along the z -axis. a_0 is the distance between the A, B sites. The lattice vectors (not shown) are given by $\mathbf{a}_1 = (a_z, -a_y)$ and $\mathbf{a}_2 = (a_z, a_y)$. The details of the model are presented in Appendix D.

E. Comparison of injection current, polarization, and strain

Fig. 4 shows the average current as a function of polarization $\mathbf{P} = \hat{\mathbf{z}}P$ for various atomic configurations of materials. For concreteness we assumed reasonable parameters, $\tau = 100$ fs[29], $\varepsilon/\varepsilon_0 \sim 4$ [10], $W = 10$ eV and used $I = \sqrt{\varepsilon/\mu} E_0^2/2$.

For a given material, the injection current susceptibility tensor is a nonmonotonic function of polarization (strain) whose absolute value reaches a local maximum at an optimal polarization $0.6P_0$ (or $\sim 9\%$ strain). The current of single-layer GeSe and GeS can change sign even with a small strain, $\sim 1\%$, suggesting a new way to engineer the injection current.

Importantly, the injection current susceptibility tensor of GeS (red) is the largest of all whereas that of SnSe is the smallest. This correlates exactly with their relative spontaneous polarizations, indicating strong correlation. Does large polarization cause the large injection current in single-layer monochalcogenides? To answer this question it would be useful to have simple model where the factors contributing to the injection current could be studied separately.

IV. TWO-BAND MODEL OF INJECTION CURRENT

The complexity of these materials makes it hard to understand the origin of the large injection current. Here we construct a simple tight-binding (TB) model which reproduces the DFT injection current susceptibility tensor near the band edge of single-layer GeS. The hopping parameters of the model are shown in Fig. 5 and more details are given in Appendix D. The injection current for a two-band model can be written as⁵

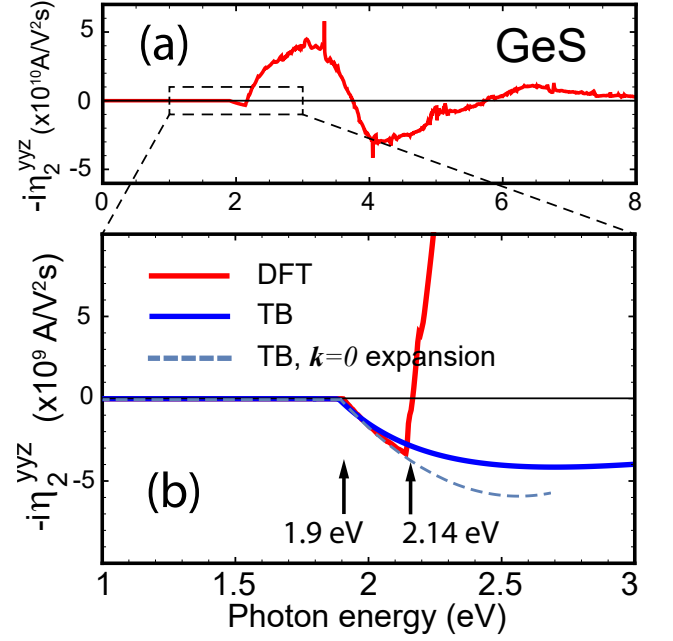


FIG. 6. Injection current of single-layer GeS from DFT and tight-binding (TB) model. The TB model captures the optical response near the band edges, in the energy range of (1.9, 2.14) eVs. For photon energies larger than 2.14 eV other regions in the BZ contribute, see Fig. 11. Dashed line shows the analytical result for a small momentum expansion about $\mathbf{k} = 0$, Eq. D14.

$$\eta_2^{yyz} = \frac{ie^3\pi}{2\hbar^2V} \sum_{\mathbf{k}} \omega_{cv,y} \Omega_c^x \delta(\omega_{cv} - \omega), \quad (9)$$

where Ω_c^x is the Berry curvature of the conduction band. Near the $\mathbf{k} = 0$ (Γ point) of the BZ, the injection current can be obtained analytically as

$$\eta_2^{yyz} = -\frac{ie^3\pi}{2\hbar^2} (\bar{\alpha}a_0 + \bar{\beta}a_z) \left(\frac{\omega - E_g}{E_g} \right) + \dots, \quad \omega \geq E_g \quad (10)$$

where $E_g = 1.89$ eV is the energy gap and $\bar{\alpha} \sim \bar{\beta} \sim 0.02$ are dimensionless constants determined by the hopping parameters. In Fig. 6 we show the injection current susceptibility tensor of a single-layer of GeS from TB and DFT calculations. In the energy range (1.9, 2.14) eV the TB model, its small $k = 0$ expansion, and the DFT results agree. For photon energies above 2.14 eV other regions of BZ contribute, see Fig. 11.

A. Origin of the injection current in the two-band model

Analysis of the form of Eq. 10 answers why the injection current is large in the model. First, the dependence

is linear in $\omega - E_g$ to lowest order and hence it grows faster than higher power exponents near the band edge. This results from the integrand being even in k_y which in turn results from $\omega_{nm,y}$ and $[r_{mn}^z, r_{nm}^y]$ each being odd under $k_y \rightarrow -k_y$. The first is a result of time reversal symmetry and the second of mirror symmetry $y \rightarrow -y$ of the crystal. Since mirror symmetries are always associated polar axes, the 2D in-plane polarization strongly constrains the frequency dependence of the injection current near the band edge.

Second, the magnitude is determined by prefactors $e^3\pi/2\hbar^2 \sim 10^{11}$ A/V²s and $(\bar{\alpha}a_0 + \bar{\beta}a_z)/d$. The first already gives a large injection current susceptibility tensor. Provided the second factor is not small we would have large injection current. The second factor is the result of the 2D integration, where d , the thickness of the slab, is used to convert to effective (bulk) values. Since a_0, a_z , and d are of the same order of magnitude, the large $\bar{\alpha}, \bar{\beta}$ are responsible for large injection current. Large $\bar{\alpha}, \bar{\beta}$ are obtained from large hopping amplitudes, arising from the covalent bonding of the Ge and S which gives the $t_1 = -2.33$ eV in our TB model³⁴.

Third, the second prefactor contains a term proportional to a_0 , the distance between the A,B sites in the model. a_0 does not enter into the band structure but it parametrizes its polarization, and hence the separation of the valence and conduction band centers of charge. As we see, it contributes about 20% of the total magnitude of the injection current. In summary, dimensionality, in-plane polarization, and covalent bonding are important factors to obtain large injection current in our TB model.

V. CONCLUSIONS

Understanding the nonlinear optical response of novel materials is of fundamental importance for advancing the field of optoelectronics. Single-layer GeSe, GeS, SnS and SnSe are predicted to exhibit promising electronic, mechanical and optical properties^{10–12}. Here we studied in details the second order effect injection current in these materials which is an important part of the bulk photovoltaic effect of any ferroelectric material. We find that the injection current is perpendicular to their in-plane spontaneous electric polarization, peaks in the visible regime, and is the biggest reported so far.

A two-band model was constructed to understand the optical response of single-layer GeS near the band edge (near Γ). The total optical response is the sum of the contributions from all of the Brillouin zone and hence is much more complicated. However, the model suggests three generic factors that may explain why injection current is so large in these materials. These are their 2D nature, in-plane polarization with associated mirror symmetries and their covalent bonding, see Fig. 1.

2D comes into play by reducing the phase space available in momentum integrations. The momentum integrals have less chance of accidental cancellations. How-

TABLE II. Band gaps and effective spontaneous polarization \mathbf{P}_0 of MM within DFT-PBE.

| Monolayer | Direct gap eV | Indirect gap eV | Polarization C/m^2 |
|-----------|------------------|--------------------|-------------------------|
| GeS | 1.89 | 1.73 | 1.95 |
| GeSe | 1.16 | 1.16 | 1.38 |
| SnS | 1.57 | 1.46 | 0.95 |
| SnSe | 0.95 | 0.95 | 0.72 |

ever 2D, alone is not always sufficient as evidenced by low injection currents produced by 2D MoS₂³⁵ or surface states of topological insulators³⁶.

The polar axis of FE materials is usually associated with mirror plane symmetries which also constrain the phase space available. However, polarization alone is not always sufficient as evidenced by the small injection current susceptibility tensors of FE CdSe, see Table I.

2D and (in-plane) polarization have the combined effects of low dimensionality and mirror symmetries. However, 2D and in-plane polarization is not sufficient because the hopping integrals can still be very small. A strong covalent bonding, however, would give large hoppings. Polarization has another benefit: it leads to valence and conduction band center separation in real space. As shown by the response at photon energies near 2.14 eV in single-layer GeS, Fig. 11, separation of the valence and conduction band centers also contributes to the magnitude of the injection current. However, polarization drives large injection currents mainly because of the symmetry constraints imposed by the in-plane polar axis on the phase space.

In summary, our results completely characterize the injection current in these novel two-dimensional ferroelectric materials. Their relatively simple structure, on one hand, and novel in-plane ferroelectrics (FE), on the other hand, make them an ideal playground for novel nonlinear optical phenomena.

VI. ACKNOWLEDGMENTS

BMF and SRP thank contract No. DE-AC02-05CH11231 and SBL the U.S. Department of Energy, Office of Basic Energy Sciences, Early Career Award DE-SC0016139.

Appendix A: Electronic band structures

The electronic band structures calculated within DFT are shown in Fig. 7 and agree with previous works³⁷. For each material, the DFT bandgaps are indicated in the figure and in Table II.

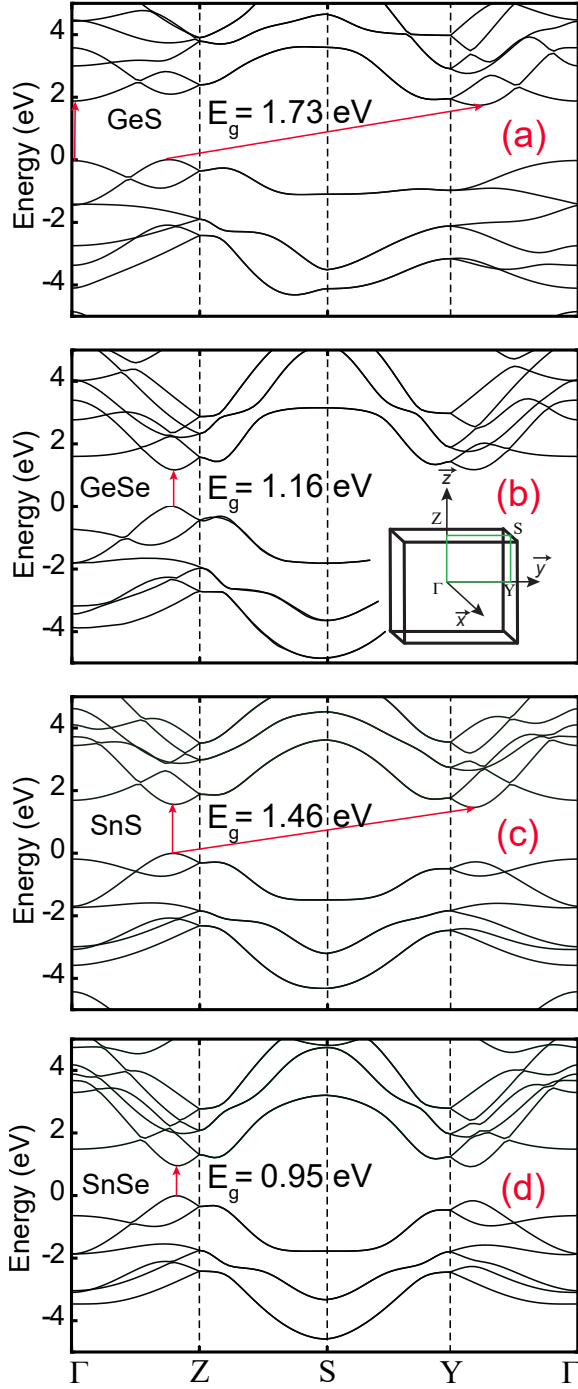


FIG. 7. Electronic bandstructure of MMs calculated within DFT-PBE. The inset indicates the path in the Brillouin zone (BZ). Red arrows indicate direct/indirect gaps.

Appendix B: Injection current and linear spectra

We used TINIBA²³ to obtain the injection current plots. Convergence was achieved with a 70×70 \mathbf{k} -point mesh, see Fig. 9. In Fig. 8, we show the yyz response of GeSe, GeS, SnS and SnSe monolayers. In all materi-

als, we see a very large response (up to 10^{10} A/V²s) in the visible light spectrum. We also show the imaginary part of the dielectric function, which controls the optical absorption of the material. Close inspection reveals that only few peaks in ε_2 correspond to peaks in η_2 (as indicated by dashed lines) and in general, there is no obvious relation between the two.

Appendix C: Electric polarization

The electric polarization of the MMs is calculated numerically²⁰ in the standard way^{32,33}

$$P^a(\lambda) = \frac{e}{V} \sum_i Z^i r_i^a(\lambda) - \frac{ie}{V} \sum_{v\mathbf{k}} \langle u_v^\lambda | u_{v,a}^\lambda \rangle, \quad (\text{C1})$$

where u_v^λ are valence Bloch wave functions, Z^i is the atomic number of the i th atom, and V is the simulation volume. λ parametrizes a smooth adiabatic path from a centrosymmetric configuration, with zero polarization, to the ground-state configuration with finite spontaneous polarization. The polarization is defined as the difference with respect to the centrosymmetric configuration.

The atomic positions in the centrosymmetric and noncentrosymmetric configurations are interpolated with straight lines under a constant area constraint¹⁵. Each atomic position is given by $\mathbf{R}^i(\lambda) = \mathbf{R}_0^i + \lambda(\mathbf{R}_f^i - \mathbf{R}_0^i)$, where \mathbf{R}_0^i (\mathbf{R}_f^i) is the initial (final) position of atom i . The use of straight lines to approximate the minimal energy path is expected to be a good approximation¹⁶. Our spontaneous polarization values ($\lambda = 1$) agrees with reports that follow a similar area constraint^{16,38}, see Table. II. For $\lambda < 1$ the polarization is also calculated as the difference with respect to the centrosymmetric configuration.

TABLE III: Positions (in Bohr) of atoms in single-layer monochalcogenides used to compute the polarization along a smooth path connecting $\mathbf{R}_f^i(\lambda = -1)$ to $\mathbf{R}_f^i(\lambda = 1)$.

GeS

Lattice parameters:

$\mathbf{a} = 28.34 \ 0.00 \ 0.00$

$\mathbf{b} = 0.00 \ 6.89 \ 0.00$

$\mathbf{c} = 0.00 \ 0.00 \ 8.52$

Atom coordinates:

| | R_0 | | | $R_f(\lambda = 1.0)$ | | | $R_f(\lambda = -1.0)$ | | |
|----|-------|------|-------|----------------------|------|-------|-----------------------|------|-------|
| Ge | 2.66 | 1.72 | -0.01 | 2.66 | 1.72 | 1.14 | 2.66 | 1.72 | -1.16 |
| Ge | 7.50 | 5.17 | 4.25 | 7.50 | 5.17 | 5.41 | 7.50 | 5.17 | 3.09 |
| S | 7.09 | 1.72 | -0.01 | 7.09 | 1.72 | -0.01 | 7.09 | 1.72 | -0.01 |
| S | 3.06 | 5.17 | 4.25 | 3.06 | 5.17 | 4.25 | 3.06 | 5.17 | 4.25 |

GeSe

$\mathbf{a} = 28.83 \ 0.00 \ 0.00$

$\mathbf{b} = 0.00 \ 7.50 \ 0.00$

$\mathbf{c} = 0.00 \ 0.00 \ 8.12$

Atom coordinates:

| | R_0 | | | $R_f(\lambda = 1.0)$ | | | $R_f(\lambda = -1.0)$ | | |
|----|-------|------|------|----------------------|------|------|-----------------------|------|-------|
| Ge | 2.98 | 2.11 | 0.16 | 2.98 | 2.11 | 0.88 | 2.98 | 2.11 | -0.55 |
| Ge | 7.57 | 5.86 | 4.22 | 7.57 | 5.86 | 4.94 | 7.57 | 5.86 | 3.5 |
| Se | 7.72 | 2.11 | 0.16 | 7.72 | 2.11 | 0.16 | 7.72 | 2.11 | 0.16 |

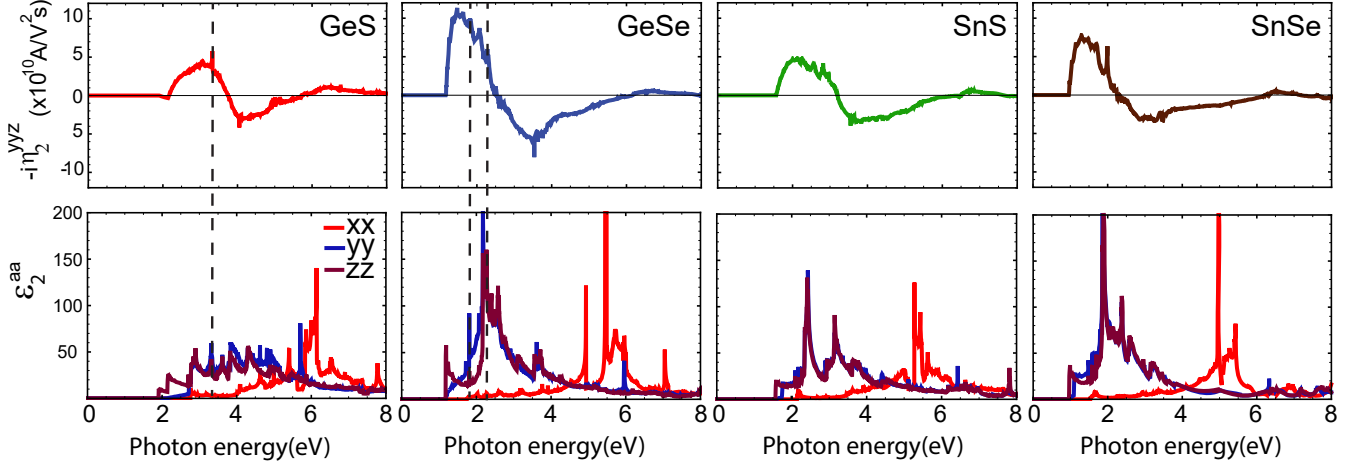


FIG. 8. (top panels) The injection current tensor of group-IV monochalcogenides monolayers. For comparison we also show the imaginary part of the linear dielectric function ϵ_2 (bottom panels) which determines the optical absorption of the material. As can be seen, there is no obvious correlation between them.

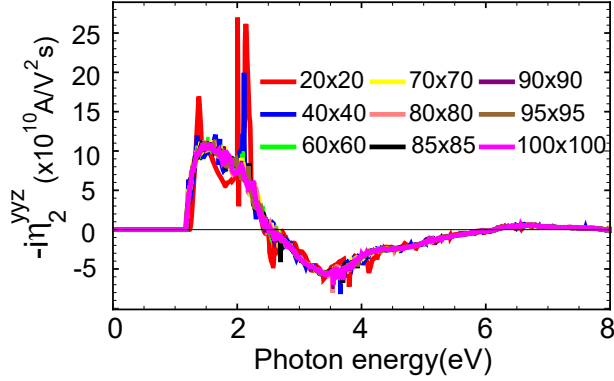


FIG. 9. Convergence of the injection current tensor for GeSe monolayer with respect to the \mathbf{k} -point mesh size.

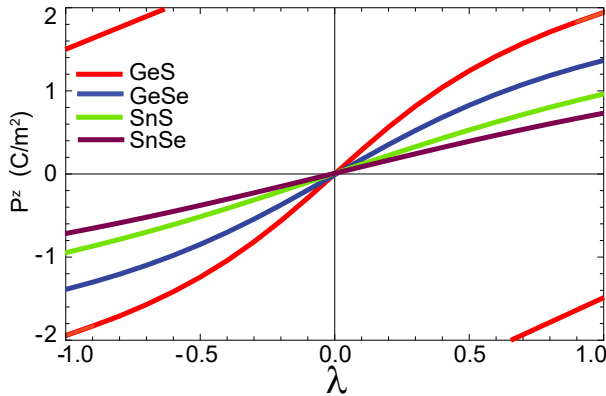


FIG. 10. Electric polarization along a path (parametrized by λ) between the asymmetric ground state $\lambda = \pm 1$ and the centrosymmetric configuration ($\lambda = 0$) on the rectangular unit cell.

| | | | | | | | | | |
|---------------------|-------|------|------|----------------------|------|------|-----------------------|------|-------|
| Se | 2.82 | 5.86 | 4.22 | 2.82 | 5.86 | 4.22 | 2.82 | 5.86 | 4.22 |
| SnS | | | | | | | | | |
| Lattice parameters: | | | | | | | | | |
| a | 28.34 | 0.00 | 0.00 | | | | | | |
| b | 0.00 | 7.72 | 0.00 | | | | | | |
| c | 0.00 | 0.00 | 8.12 | | | | | | |
| Atom coordinates: | | | | | | | | | |
| | R_0 | | | $R_f(\lambda = 1.0)$ | | | $R_f(\lambda = -1.0)$ | | |
| Sn | 2.73 | 1.93 | 0.31 | 2.73 | 1.93 | 0.94 | 2.73 | 1.93 | -0.30 |
| Sn | 8.12 | 5.79 | 4.37 | 8.12 | 5.79 | 5.00 | 8.12 | 5.79 | 3.75 |
| S | 7.60 | 1.93 | 0.31 | 7.60 | 1.93 | 0.31 | 7.60 | 1.93 | 0.31 |
| S | 3.25 | 5.79 | 4.37 | 3.25 | 5.79 | 4.37 | 3.25 | 5.79 | 4.37 |
| SnSe | | | | | | | | | |
| Lattice parameters: | | | | | | | | | |
| a | 28.34 | 0.00 | 0.00 | | | | | | |
| b | 0.000 | 8.11 | 0.00 | | | | | | |
| c | 0.000 | 0.00 | 8.31 | | | | | | |
| Atom coordinates: | | | | | | | | | |
| | R_0 | | | $R_f(\lambda = 1.0)$ | | | $R_f(\lambda = -1.0)$ | | |
| Sn | 2.98 | 2.11 | 0.29 | 2.98 | 2.11 | 0.71 | 2.98 | 2.11 | -0.13 |
| Sn | 8.19 | 6.16 | 4.44 | 8.19 | 6.16 | 4.87 | 8.19 | 6.16 | 4.01 |
| Se | 8.12 | 2.11 | 0.29 | 8.12 | 2.11 | 0.29 | 8.12 | 2.11 | 0.29 |
| Se | 3.05 | 6.17 | 4.44 | 3.05 | 6.17 | 4.44 | 3.05 | 6.17 | 4.44 |

Appendix D: Two-band model of the injection current of single-layer GeS

We consider a two-band Hamiltonian

$$H = f_0 \sigma_0 + f_a \sigma_a, \quad (\text{D1})$$

where $\sigma_a, a = x, y, z$ are the standard Pauli matrices and σ_0 is the 2×2 identity matrix. Summation over repeated indices is implied. The functions f_a are given by the hopping integrals of the model. The Hamiltonian has

eigenvectors given by

$$u_c = A \begin{pmatrix} f_x - if_y \\ \epsilon - f_z \end{pmatrix} \quad (D2)$$

$$u_v = A \begin{pmatrix} f_z - \epsilon \\ f_x + if_y \end{pmatrix}, \quad (D3)$$

where $A^{-2} = 2\epsilon(\epsilon - f_z)$ is the normalization and eigenvalues by $E_{c,v} = f_0 \pm \epsilon$ where $\epsilon = \sqrt{f_a f_a}$ and c, v denote the conduction and valence band respectively. An arbitrary phase factor has been omitted, since the final expression is independent of this phase (gauge). The Bloch wave functions are constructed as

$$\psi_{n\mathbf{k}} = \sum_{\mathbf{R}} e^{i\mathbf{k} \cdot \mathbf{R}} [u_n^{(1)} \phi(\mathbf{r} - \mathbf{R}) + e^{i\mathbf{k} \cdot \mathbf{r}_0} u_n^{(2)} \phi(\mathbf{r} - \mathbf{r}_0 - \mathbf{R})], \quad (D4)$$

where $u_n^{(i)}$ denotes the eigenvector corresponding to eigenvalue $n = v, c$ (valence, conduction) and $i = 1, 2$ denotes the first and second components. $\mathbf{r}_0 = (a_0, 0)$ is the position of site B with respect to site A which is taken to be the origin. $\phi(\mathbf{r})$ are p_x -orbitals and \mathbf{R} runs over all lattice positions. Notice that the phase of the wave function at site B is different than that at site A .

Let us compute matrix elements in the expression for η_2^{yyz} of the two-band model. This has been done before⁵ following Ref. 4. Here we present a simpler derivation. Denoting $X_{,a} \equiv \partial X / \partial k_a$ and using the definition of the Berry connection, $r_{nm}^a = i \langle u_n | u_{m,a} \rangle$, we have

$$r_{cv}^z r_{vc}^y - r_{cv}^y r_{vc}^z = -\langle u_c | u_{v,z} \rangle \langle u_v | u_{c,y} \rangle + \langle u_c | u_{v,y} \rangle \langle u_v | u_{c,z} \rangle. \quad (D5)$$

Transfer derivatives from the ket to the bra at the expense of a minus sign by taking derivatives of $\langle u_n | u_m \rangle = \delta_{nm}$. Substituting the identity $1 = |u_v\rangle \langle u_v| + |u_c\rangle \langle u_c|$ we obtain

$$r_{cv}^z r_{vc}^y - r_{cv}^y r_{vc}^z = \langle u_{c,z} | u_{c,y} \rangle - \langle u_{c,y} | u_{c,z} \rangle \equiv i\Omega_c^x, \quad (D6)$$

where in the 1st line we used $\langle u_{c,z} | u_c \rangle \langle u_c | u_{c,y} \rangle = \langle u_{c,y} | u_c \rangle \langle u_c | u_{c,z} \rangle$ and in the last line the definition of the Berry curvature $\Omega_n^a = i\epsilon_{abc} \langle u_{n,b} | u_{n,c} \rangle$.

In general, one can show⁴

$$\Omega_n^a = i\epsilon_{abc} \sum_{m \neq n} r_{nm}^b r_{mn}^c, \quad (D7)$$

where ϵ_{abc} is the levi-civita tensor in three dimensions. In a two-band model the sum over bands has only one term and the injection current susceptibility tensor gives

$$\eta_2^{yyz} = \frac{ie^3\pi}{2\hbar^2 V} \sum_{\mathbf{k}} \omega_{cv,y} \Omega_c^x \delta(\omega_{cv} - \omega), \quad (D8)$$

which is the Eq. 9 of the main text. The Berry curvature in term of the f 's is $\Omega_c^a = \epsilon_{abc} \epsilon_{ajk} (A^2 f_i)_{,b} f_{j,k,c}$.

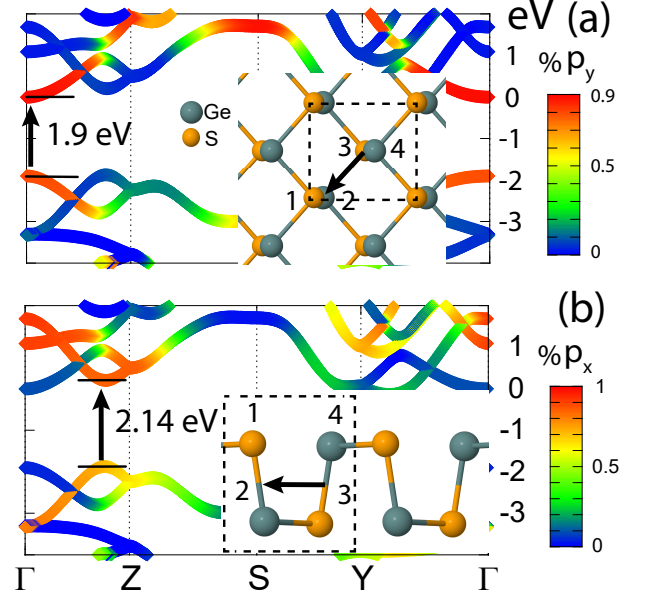


FIG. 11. Band projections into localized hydrogenic s, p states for each of the Ge and S atoms in single-layer GeS. The states are centered at atomic positions 1-4 (inset). In (a) we show that the bands near the Γ point in the BZ are mostly of p_y -character. However, the location of the valence and conduction band centers are at atomic positions 3,4 and 1,2 respectively. Hence the photoexcited carrier moves in real space within the unit cell. In (b) we show that the bands near the Z point are mostly of p_x -character and that their valence and conduction band centers are also separated in real space. The transition at photon energies 2.14 eV gives a very large injection current contribution, suggesting valence/conduction center separation plays an important role.

1. Parameters of single-layer GeS

The Hamiltonian of the model is given by³⁴

$$f_0 = 2t'_1 [\cos \mathbf{k} \cdot \mathbf{a}_1 + \cos \mathbf{k} \cdot \mathbf{a}_2] + 2t'_2 \cos \mathbf{k} \cdot (\mathbf{a}_1 - \mathbf{a}_2), \quad (D9)$$

$$f_x - if_y = e^{i\mathbf{k} \cdot \mathbf{r}_0} (t_1 + t_2 \Phi_{\mathbf{k}} + t_3 \Phi_{\mathbf{k}}^*), \quad (D10)$$

$$f_z = \Delta, \quad (D11)$$

where $\Phi_{\mathbf{k}} \equiv e^{-i\mathbf{k} \cdot \mathbf{a}_1} + e^{-i\mathbf{k} \cdot \mathbf{a}_2}$, Δ is the onsite potential and $t_1, t_2, t_3, t'_1, t'_2$ are hopping matrix elements as indicated in Fig. 5. $\mathbf{a}_1 = (a_z, -a_y)$, $\mathbf{a}_2 = (a_z, a_y)$ are the primitive lattice vectors. Note that f_0 and hence t'_1, t'_2 do not enter into the injection current.

For concreteness we use TB parameters corresponding to single-layer GeS: $(a_z, a_y, d) = (4.53/2, 3.63/2, 2.56)$ Å, where d is the thickness of the slab, $a_0 = 0.62$ Å, and $(t_1, t_2, t_3, t'_1, t'_2, \Delta) = (-2.33, 0.61, 0.13, 0.07, -0.09, -0.41)$ eV. It was shown that these parameters reproduce the band structure and geometry of the wavefunction in the vicinity of the Gamma point³⁴. To compare with bulk values obtained

from the DFT calculations the results of the TB model are multiplied by $2/d$. The factor of 2 accounts for the smaller TB unit cell.

2. Injection current near band edge of single-layer GeS

An analytic expression for the injection current susceptibility tensor can be obtained for small momenta near $\mathbf{k} = 0$. The delta function fixes the energy and the remaining integral can be done easily for a quadratic band. ω_{cv} and the Berry curvature are

$$\hbar\omega_{cv} = E_g + \alpha a_z^2 k_z^2 + \beta a_y^2 k_y^2 + \gamma a_z^2 a_y^2 k_z^2 k_y^2 + \dots$$

$$\Omega_c^x = -(Aa_0 + Ba_z)a_y^2 k_y - Ca_y a_z^2 k_y k_z^2 + \dots, \quad (\text{D12})$$

where $E_g = 1.89$ eV is the energy gap and $\alpha = 2.3, \beta = 1.3, \gamma = -2.1, A = 0.30, B = 0.34$ are dimensionless constants that depend on the hopping parameters. C depends on the lattice parameters also. Note the Berry curvature is odd under $k_y \rightarrow -k_y$. This is a general

property of $r_{nm}^a r_{mn}^b - r_{nm}^b r_{mn}^a$ when either a or b is equal to y and arises due to the mirror plane symmetry $y \rightarrow -y$ of the crystal. Because of this symmetry the integrand in Eq. D8 is even in k_y (proportional to k_y^2 to the lowest order) giving rise to a linear term $\omega - E_g$. Indeed, after integration we obtain

$$\eta_2^{yyz} = -\frac{ie^3\pi}{2\hbar^2} \left[\frac{(Aa_0 + Ba_z)a_y}{4\pi a_z \sqrt{\alpha\beta}} (\omega - E_g) + \frac{(\beta C + \gamma(Aa_0 + Ba_z)a_y)}{16\pi a_z \sqrt{\alpha\beta\alpha\beta}} (\omega - E_g)^2 + \dots \right], \quad (\text{D13})$$

for $\omega \geq E_g$. Substituting numerical values we obtain

$$\eta_2^{yyz} = -\frac{ie^3\pi}{2\hbar^2} \left[0.07\text{\AA} \left(\frac{\omega - E_g}{E_g} \right) - 0.07\text{\AA} \left(\frac{\omega - E_g}{E_g} \right)^2 + \dots \right]. \quad (\text{D14})$$

η_2^{yyz} is plotted in Fig. 6 after converting into bulk values.

-
- ¹ B. I. Sturman and P. J. Sturman, *Photovoltaic and Photo-refractive Effects in Noncentrosymmetric Materials* (CRC Press, 1992).
 - ² A. M. Rappe, I. Grinberg, and J. E. Spanier, *Proceedings of the National Academy of Sciences* **114**, 7191 (2017).
 - ³ J. Rioux and J. Sipe, *Physica E: Low-dimensional Systems and Nanostructures* **45**, 1 (2012).
 - ⁴ J. E. Sipe and A. I. Shkrebtii, *Phys. Rev. B* **61**, 5337 (2000).
 - ⁵ F. de Juan, A. G. Grushin, T. Morimoto, and J. E. Moore, *Nature Communications* **8**, 15995 (2017).
 - ⁶ C. Paillard, G. Geneste, L. Bellaiche, J. Kreisel, M. Alexe, and B. Dkhil, "Emerging photovoltaic materials," (Wiley & Sons Ltd, 2018) Chap. 2, p. 105.
 - ⁷ R. von Baltz and W. Kraut, *Phys. Rev. B* **23**, 5590 (1981).
 - ⁸ J. E. Spanier, V. M. Fridkin, A. M. Rappe, A. R. Akbashev, A. Polemi, Y. Qi, Z. Gu, S. M. Young, C. J. Hawley, D. Imbrenda, G. Xiao, A. L. Bennett-Jackson, and C. L. Johnson, *Nat. Photonics* **10**, 611 (2016).
 - ⁹ A. M. Burger, R. Agarwal, A. Aprelev, E. Schrubba, A. Gutierrez-Perez, V. M. Fridkin, and J. E. Spanier, *Science Advances* **5** (2019).
 - ¹⁰ L. C. Gomes and A. Carvalho, *Phys. Rev. B* **92**, 085406 (2015).
 - ¹¹ G. G. Naumis, S. Barraza-Lopez, M. Oliva-Leyva, and H. Terrones, *Reports on Progress in Physics* **80**, 096501 (2017).
 - ¹² T. Hu and E. Kan, *Wiley Interdisciplinary Reviews: Computational Molecular Science* **0**, e1409 (2019).
 - ¹³ K. Chang, J. Liu, H. Lin, N. Wang, K. Zhao, A. Zhang, F. Jin, Y. Zhong, X. Hu, W. Duan, Q. Zhang, L. Fu, Q.-K. Xue, X. Chen, and S.-H. Ji, *Science* **353**, 274 (2016).
 - ¹⁴ M. Mehboudi, B. M. Fregoso, Y. Yang, W. Zhu, A. van der Zande, J. Ferrer, L. Bellaiche, P. Kumar, and S. Barraza-Lopez, *Phys. Rev. Lett.* **117**, 246802 (2016).
 - ¹⁵ S. Barraza-Lopez, T. P. Kaloni, S. P. Poudel, and P. Kumar, *Phys. Rev. B* **97**, 024110 (2018).
 - ¹⁶ T. Rangel, B. M. Fregoso, B. S. Mendoza, T. Morimoto, J. E. Moore, and J. B. Neaton, *Phys. Rev. Lett.* **119**, 067402 (2017).
 - ¹⁷ B. M. Fregoso, T. Morimoto, and J. E. Moore, *Phys. Rev. B* **96**, 075421 (2017).
 - ¹⁸ K. Kushnir, M. Wang, P. D. Fitzgerald, K. J. Koski, and L. V. Titova, *ACS Energy Letters* **2**, 1429 (2017).
 - ¹⁹ K. Kushnir, Y. Qin, Y. Shen, G. Li, B. M. Fregoso, S. Tongay, and L. V. Titova, *ACS Applied Materials & Interfaces* **11**, 5492 (2019).
 - ²⁰ X. Gonze *et al.*, *Computer Physics Communications* **180**, 2582 (2009).
 - ²¹ J. P. Perdew, K. Burke, and Y. Wang, *Phys. Rev. B* **54**, 16533 (1996).
 - ²² C. Hartwigsen, S. Goedecker, and J. Hutter, *Phys. Rev. B* **58**, 3641 (1998).
 - ²³ TINIBA is a tool written in bash, perl, and fortran to compute optical responses based on the ABINIT. <https://github.com/bemese/tiniba>.
 - ²⁴ P. E. Blöchl, O. Jepsen, and O. K. Andersen, *Phys. Rev. B* **49**, 16223 (1994).
 - ²⁵ N. Laman, A. I. Shkrebtii, J. E. Sipe, and H. M. van Driel, *Applied Physics Letters* **75**, 2581 (1999).
 - ²⁶ M. E. Schmidt, S. A. Blanton, M. A. Hines, and P. Guyot-Sionnest, *The Journal of Chemical Physics* **106**, 5254 (1997).
 - ²⁷ F. Nastos and J. E. Sipe, *Phys. Rev. B* **82**, 235204 (2010).
 - ²⁸ N. Laman, M. Bieler, and H. M. van Driel, *Journal of Applied Physics* **98**, 103507 (2005).
 - ²⁹ G. Li, K. Kushnir, M. Wang, Y. Dong, S. Chertopalov, A. M. Rao, V. N. Mochalin, R. Podila, K. Koski, and L. V.

- Titova, in *2018 43rd International Conference on Infrared, Millimeter, and Terahertz Waves (IRMMW-THz)* (2018).
- ³⁰ M. Pagliaro, G. Palmisano, and R. Ciriminna, *Flexible Solar Cells* (John Wiley & Sons, Ltd, 2008).
- ³¹ R. W. Boyd, *Nonlinear Optics* (Academic Press, 2008).
- ³² R. D. King-Smith and D. Vanderbilt, Phys. Rev. B **47**, 1651 (1993).
- ³³ R. Resta, Rev. Mod. Phys. (1994).
- ³⁴ A. M. Cook, B. M. Fregoso, F. de Juan, S. Coh, and J. E. Moore, Nature Communications **8**, 14176 (2017).
- ³⁵ R. A. Muniz and J. E. Sipe, Phys. Rev. B **89**, 205113 (2014).
- ³⁶ D. A. Bas, R. A. Muniz, S. Babakiray, D. Lederman, J. E. Sipe, and A. D. Bristow, Opt. Express **24**, 23583 (2016).
- ³⁷ A. K. Singh and R. G. Hennig, Applied Physics Letters (2014).
- ³⁸ R. Fei, W. Kang, and L. Yang, Phys. Rev. Lett. **117**, 097601 (2016).